Atmospheric Research 240 (2020) 104946

Contents lists available at ScienceDirect

Atmospheric Research

journal homepage: www.elsevier.com/locate/atmosres

Evaluation of land-atmosphere processes of the Polar WRF in the summertime Arctic tundra

Jeongwon Kim[a], Junhong Lee[a,2], Je-Woo Hong[b], Jinkyu Hong[a,*], Ja-Ho Koo[c], Joo-Hong Kim[d], Juyeol Yun[d,1], Sungjin Nam[d], Ji Young Jung[d], Taejin Choi[d], Bang Yong Lee[d]

[a] Ecosystem-Atmosphere Process Laboratory, Department of Atmospheric Sciences, Yonsei University, Seoul, Republic of Korea
[b] Korea Environment Institute, Sejong, Republic of Korea
[c] Atmospheric Chemistry Lab, Department of Atmospheric Sciences, Yonsei University, Seoul, Republic of Korea
[d] Korea Polar Research Institute, Incheon, Republic of Korea

ARTICLE INFO

Keywords:
Polar WRF
Arctic tundra
Land-atmosphere interaction
Surface energy balance
Soil moisture
Planetary boundary layer

ABSTRACT

Arctic tundra is undergoing a rapid transition due to global warming and will be exposed to snow-free conditions for longer periods under projected climate scenarios. Regional climate modeling is useful for understanding and predicting climate change in the Arctic tundra, however, the lack of in-situ observations of surface energy fluxes and the planetary boundary layer (PBL) structure hinders accurate predictions of local and regional climate around the Arctic. In this study, we investigate the performance of the Polar-optimized version of the Weather Research and Forecasting model (PWRF) in the Arctic tundra on clear days in summer. Based on simultaneous observations of surface fluxes and the PBL structure in Cambridge Bay, Nunavut, Canada, our validation shows that the PWRF simulates a drier environment, leading to a larger Bowen ratio and a warmer atmosphere compared to observations. Further sensitivity analyses indicate that the model biases are mainly from the uncertainties in physical parameters such as surface albedo and emissivity, the solar constant, and the model top height, rather than structural flaws in the model physics. Importantly, the PWRF reproduces the observations more accurately when the observed soil moisture is fed into the simulation. This indicates that there must be improvements in simulations of the land-atmosphere interaction at the Arctic tundra, not only in the accuracy of the initial soil moisture conditions but also in soil hydraulic properties and drainage processes. The mixing diagram analysis also shows that the entrainment process between the PBL and the overlying atmosphere needs to be improved for better weather and climate simulation. Our findings shed light on modeling studies in the Arctic region by disentangling the model error sources from uncertainties by parameters and physics package options.

1. Introduction

The Arctic environment has been changing rapidly in recent decades due to climate change (Cavalieri and Parkinson, 2012; Comiso et al., 2008). In particular, Arctic tundra is undergoing a substantial transition due to extensive permafrost thawing and subsequent vegetation changes with global warming (e.g., Elmendorf et al., 2012; Goetz et al., 2010; Henry and Molau, 1997). Permafrost thawing is likely to accelerate global warming by releasing carbon stored in the soil to the atmosphere (Anisimov, 2007; Christensen et al., 2004). Its impacts on weather and climate will not be confined to the Arctic region but will extend to the mid-latitudes of the Northern Hemisphere where almost 90% of the global population lives (Cohen et al., 2014; Overland et al., 2015). Consequently, it is essential to improve our understanding of environmental change at the Arctic tundra and its interplay with local and regional climate in a changing climate.

In the Arctic, several regional and global modeling studies have been conducted in the last two decades, leading to the better model performance (e.g., Bromwich et al., 2018; Hines et al., 2011; Lynch et al., 1995, 1998; Roberts et al., 2010). Recently, a Polar-optimized version of the Weather Research and Forecasting model (PWRF hereafter) was developed by the Polar Meteorology Group (Hines and

* Corresponding author at: Ecosystem-Atmosphere Process Laboratory, Department of Atmospheric Sciences, Yonsei University, Yonsei-ro 50, Seodaemun-gu, Seoul 03722, Republic of Korea.
E-mail address: jhong@yonsei.ac.kr (J. Hong).
[1] Current affiliation: Korea Atomic Energy Research Institute, Daejeon, Republic of Korea.
[2] Current affiliation: Max Planck Institute for Meteorology, Hamburg, Germany.

https://doi.org/10.1016/j.atmosres.2020.104946
Received 31 October 2019; Received in revised form 28 February 2020; Accepted 8 March 2020
Available online 09 March 2020

Bromwich, 2008) as the Weather Research and Forecasting model (WRF) optimized for Arctic and Antarctic regions. As a regional climate modeling framework, the PWRF has facilitated studies of weather and climate in polar regions at a high-resolution in various surface environments including ice-sheet, ocean, land, and sea ice across the Arctic domain and has been applied for the Arctic System Reanalysis over the entire Arctic region. (e.g., Bromwich et al., 2009, 2018; Hines and Bromwich, 2008; Hines et al., 2011, 2015; Wilson et al., 2011, 2012). The PWRF places emphasis on sea ice and snow-covered surfaces that cover the Arctic throughout the year, except during a short summer season. From this perspective, despite improvements of the PWRF during the last decade, its use is limited for studies in tundra environments. Importantly, in the future, snow-free tundra will expand in the Arctic region with global warming and be exposed to snow-free conditions for longer periods in the future (Serreze and Barry, 2014). Arctic tundra may exert greater effects on local and regional weather and climate if global warming intensifies (Chapin III et al., 2000). Accordingly, accurate atmospheric simulation around the Arctic tundra is of great concern for improving predictions and assessments of repercussions of change in the Arctic tundra on our sustainability (Hinzman et al., 2005). The PWRF does not successfully capture several key aspects of surface energy exchanges and boundary layer structure in this critical area (Hines et al., 2011) and the lack of in-situ observations, as a result of limited accessibility due to the extreme climate conditions, further hinders evaluations of land-atmosphere processes in this region.

Few studies have evaluated regional or global climate models over the Arctic tundra based on in-situ observation. Hines et al. (2011) evaluated the overall forecast performance of the PWRF across Alaska in abrupt spring snow melt during the winter to summer transition especially on the North Slope. Bromwich et al. (2018) expanded the PWRF modeling system across Arctic tundra in the Arctic System Reanalysis. Despite their prominent findings on the PWRF performance in the Arctic tundra, previous studies were limited by a relatively coarse horizontal grid size of 25 km which was larger than the observation footprint. Indeed, the second-nearest land grid to the observation site was selected for comparison because the nearest grid was classified as an ocean grid. The lack of simultaneous observations of the surface energy balance (SEB) and planetary boundary layer (PBL) structure also limited our understanding of the drawbacks of the model in simulating changes of Arctic tundra and the impacts on weather and climate (Eugster et al., 2000). The model bias of cloud simulation was mixed up with errors to simulate the SEB because clear and cloudy days were not analyzed separately and the impacts of uncertainties in parameters predefined in the model had not been extensively investigated.

The present study investigated the performance of PWRF in Arctic tundra to simulate the SEB and PBL structure on clear summer days in July of 2012. We focused on the PWRF performance and modeling uncertainties in surface parameters and physical parameterization on clear days because bias in clouds makes substantial errors in simulating the SEB and PBL structure. This enabled the determination of the sources of modeling errors. We examined the overall performance of the PWRF based on in-situ observations of the SEB and PBL structure by eddy covariance and radiosonde sounding measurements. Then, a series of sensitivity experiments was conducted to quantify the modeling error by uncertainties in a few key parameters and physics parameterization, and eventually to improve model simulations for weather and climate prediction.

2. Materials and methods

2.1. Site description and measurements

This study used surface meteorological data observed at the Cambridge Bay (CBB) site in Nunavut, Canada, operated by the Korea Polar Research Institute (69°07′47″N, 105°03′35″W, 15 m above m.s.l.) (Fig. 1). We also used an upper air measurement data from the station near the CBB station operated by the Environment Canada (69°07′59″N, 105°03′59″W). The vegetation cover around the CBB site is mainly covered with dwarf-shrubs, graminoids, and lichens, and is classified as mixed tundra in the model, consistently (Fig. 1c). For most of the year, the ground of CBB is covered with snow. In the summer season from June to August, snow melts and the top soil layer on the permafrost thaws (called the active layer that usually freezes in winter and thaws in summer). The active layer is deepened with the warming conditions, thus leading to a change in hydrological process of CBB (Calihoo and Romaine, 2010). During the simulation period, it was clear under the influence of the high-pressure system and there was no sea ice around the CBB station based on the ERA-Interim reanalysis data. It is also notable that the Arctic sea ice had rapidly decreased in summer 2012 compared to normal years in response to dramatic warming and arctic storm (Beitler, 2012; Parkinson and Comiso, 2013). The monthly mean air temperature and precipitation in July of 2012 were significantly higher than the 30-year averages (from 1985 to 2015), thus indicating suitable conditions for the model evaluation in a climate affected by global warming. The 30-year averaged July mean air temperature and precipitation around the CBB station were 9.0 °C and 14.1 mm month^{-1}, respectively. The monthly mean air temperature, precipitation, and soil moisture in July 2012 were 10.8 °C, 53.9 mm month^{-1}, and 0.28 m^3 m^{-3}, respectively (source: Environment and Climate Change Canada: https://climate.weather.gc.ca).

For the model evaluation, this study used the 30-min interval data of surface meteorological variables and 12-h interval data by radiosonde observation (00 UTC, 12 UTC) from 3 to 10 July 2012. The surface-observed variables included downward and upward shortwave radiation ($K_\downarrow$ and $K_\uparrow$), downward and upward longwave radiation ($L_\downarrow$ and $L_\uparrow$), sensible heat flux (H), latent heat flux (LE), 5-m air temperature (T_5), and 5-m wind speed (U_5) (Table 3), and the radiosonde observed variables included potential temperature (θ), and water vapor mixing ratio. Surface radiative fluxes and surface energy fluxes were measured directly by a net radiometer (CNR4, Kipp and Zonen, Netherlands) and an eddy-covariance system (CSAT3, Campbellsci, Inc., USA; EC150, Campbellsci, Inc., USA), respectively. For our model evaluation, we allocated the surface energy imbalance to the observed heat fluxes (i.e., H and LE) based on the Bowen ratio ($\beta \equiv H/LE$) following Twine et al. (2000). More information on the observation data can be found at the Korea Polar Data Center (https://kpdc.kopri.re.kr) and in Lee (2018).

2.2. Model description

The PWRF version 3.8.1 was used in this study to evaluate the performance to simulate surface and boundary layer properties over the tundra surface around the CBB site (Table 1). The physics package of the control (CTL) simulation included the Morrison 2-moment scheme for cloud microphysics, Mellor–Yamada–Janjić (MYJ) PBL scheme, Eta similarity scheme for the surface layer, Goddard shortwave radiation scheme, rapid radiative transfer scheme for general circulation models (RRTMG) longwave radiation scheme, and Noah land surface model (Hines et al., 2011 and references therein). The Grell–Dévényi cumulus parameterization was used in the first and second domains and turned off for the domains of which the horizontal resolution was smaller than 4 km (Weisman et al., 1997). All the options related to the sea ice were prescribed as default settings in the PWRF.

One-way of four-nested domains with a Lambert conformal map projection was used for high-resolution simulation because target area is the tundra region in regional scales rather than the entire Arctic area (Fig. 1a). Each domain had 46 × 46 grids and the horizontal resolutions were 27 km, 9 km, 3 km, and 1 km, respectively. The vertical layer consisted of 31 levels up to 50 hPa. The simulation period was set to 9 days (1–10 July 2012) including a 48-h spin-up period, and our analysis focused on the last seven days. During most of the study period, the clear-sky was relatively long-lasting under the influence of a high-pressure system. Our analysis excluded the period when there was

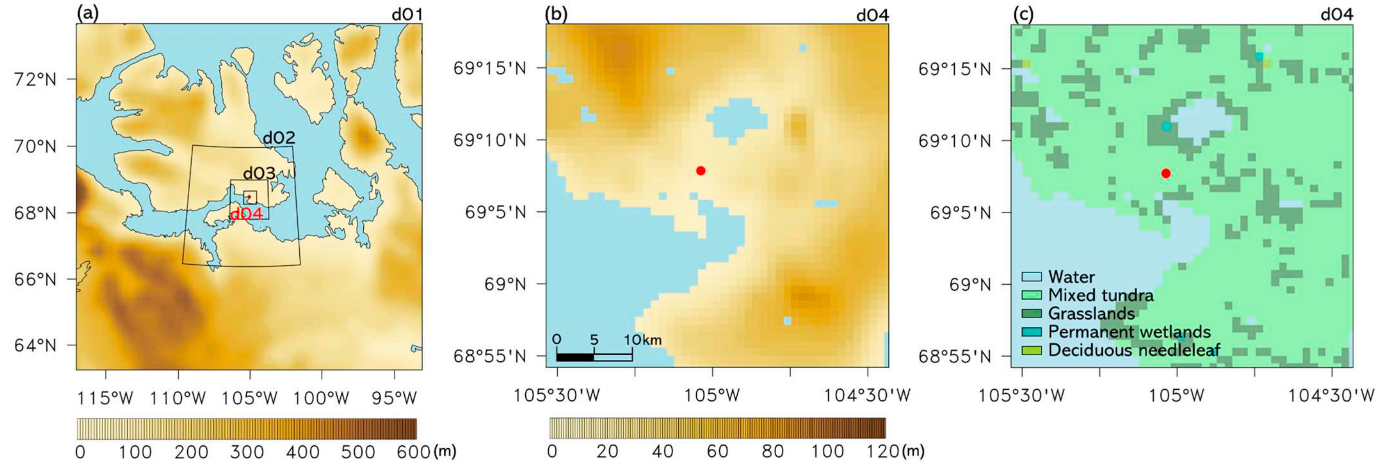

Fig. 1. Domain composition for the PWRF experiments showing (a) topographical map for all domains and (b) for domain 4 specifically, and (c) vegetatin cover for domain 4. Each domain had 46 × 46 grids and the horizontal resolutions were 27 km, 9 km, 3 km, and 1 km, respectively. The observation site of Cambridge Bay, Nunavut, Canada is marked with red point (69°07′47″N, 105°03′35″W). (For interpretation of the references to colour in this figure legend, the reader is referred to the web version of this article.)

Table 1
The numerical model settings and physics package of the CTL experiment.

CTL experiment	
Version	Polar WRF ver.3.8.1
Periods	1–10 July 2012 (spin-up: 48 h)
Initial & Boundary condition	ERA-Interim
Horizontal resolutions	27, 9, 3, 1 km (4 domains with 1-way nesting)
Vertical resolutions	31 layers (up to 50 hPa)
Grids	46 × 46 (for each domain)
Physics	
Microphysics	Morrison 2-moment scheme
PBL physics	Mellor–Yamada-Janjić (MYJ) scheme
Surface layer physics	Eta similarity scheme
Radiation physics	Goddard scheme (Shortwave radiation) RRTMG scheme (Longwave radiation)
Cumulus physics	Grell - Dévényi ensemble scheme (domain 1 & 2 only)
Land surface model	Noah LSM

observed precipitation of 2 mm day^{-1} to focus only on the surface processes on clear summer days. The PWRF did not make cloud liquid water and cloud ice during the simulation period except on these excluded days. For the initial and boundary conditions, the 6-hourly ERA-Interim data was used, which is provided by the European Centre for Medium-Range Weather Forecasts. Air temperature correction for topography was not applied because the terrain height difference was less than 10 m between observations and the model.

Additional numerical experiments were performed with different physical constants and parameterizations to quantify the impacts of uncertainties in parameters that influenced the SEB and the PBL structure (Table 2 and Table S1). In the RAD simulation, the RRTMG scheme was applied for shortwave radiation physics instead of the Goddard shortwave scheme. Additional sensitivity experiments were conducted in the CTL and RAD simulations to quantify uncertainties in $K_{\downarrow}$: (i) an increase in the model top from 50 hPa to 1 hPa to consider the radiation absorption by ozone in the upper atmosphere, (ii) a decrease in the solar constant from the default value (i.e., 1370 W m^{-2}) to 1361 W m^{-2}, which was observed from the Solar Radiation and Climate Experiment (SORCE) satellite in the simulation period (Woods et al., 2000). In the SFC simulation, the surface albedo and emissivity were adjusted to the observed values reported by Langer et al. (2010, 2011) and Wilber et al. (1999). In the MTS simulation, soil moisture of top soil layer was fixed to the observed mean of soil moisture at the CBB site by increasing the value from the CTL simulation.

For the model validation, the standard deviation, centered root-–mean–square error (RMSE), and correlation coefficients of the model normalized by their corresponding values of the observation are together shown in a Taylor diagram (Taylor, 2001). Accordingly, a point nearer the observation at a reference point (OBS) indicates a better agreement with the observation in the Taylor diagram. The normalized bias by the corresponding mean values of the observation was also shown in the Taylor diagram based on Elvidge et al. (2014).

3. Results and discussion

3.1. Evaluation of land-atmosphere processes in CTL experiment

Fig. 2 shows the mean diurnal patterns of surface variables from the tower observation and the model simulations during the simulation

Table 2
The abbreviations of sensitivity simulations conducted in the study and their numerical design features.

Abbreviation	Description
CTL_M	Model top increases from 50 to 1 hPa (Other settings are same as the CTL experiment).
CTL_S	Solar constant decreases from 1370 to 1361 W m^{-2} (Other settings are same as the CTL experiment).
CTL_MS	Both increased model top and decreased solar constant are applied (Other settings are same as the CTL experiment).
RAD	The Goddard scheme is replaced by the RRTMG scheme for shortwave radiation physics (Other settings are same as the CTL experiment).
RAD_M	Model top increases from 50 to 1 hPa (Other settings are same as the RAD experiment).
RAD_S	Solar constant decreases from 1370 to 1361 W m^{-2} (Other settings are same as the RAD experiment).
RAD_MS	Both increased model top and decreased solar constant are applied (Other settings are same as the RAD experiment).
SFC	Surface albedo and emissivity change to 0.20 and 0.98, respectively (Other settings are same as the RAD experiment).
MTS	Soil moisture in the top soil layer is fixed to 0.28 m^3 m^{-3} in domain 4 (Other settings are same as the SFC experiment).

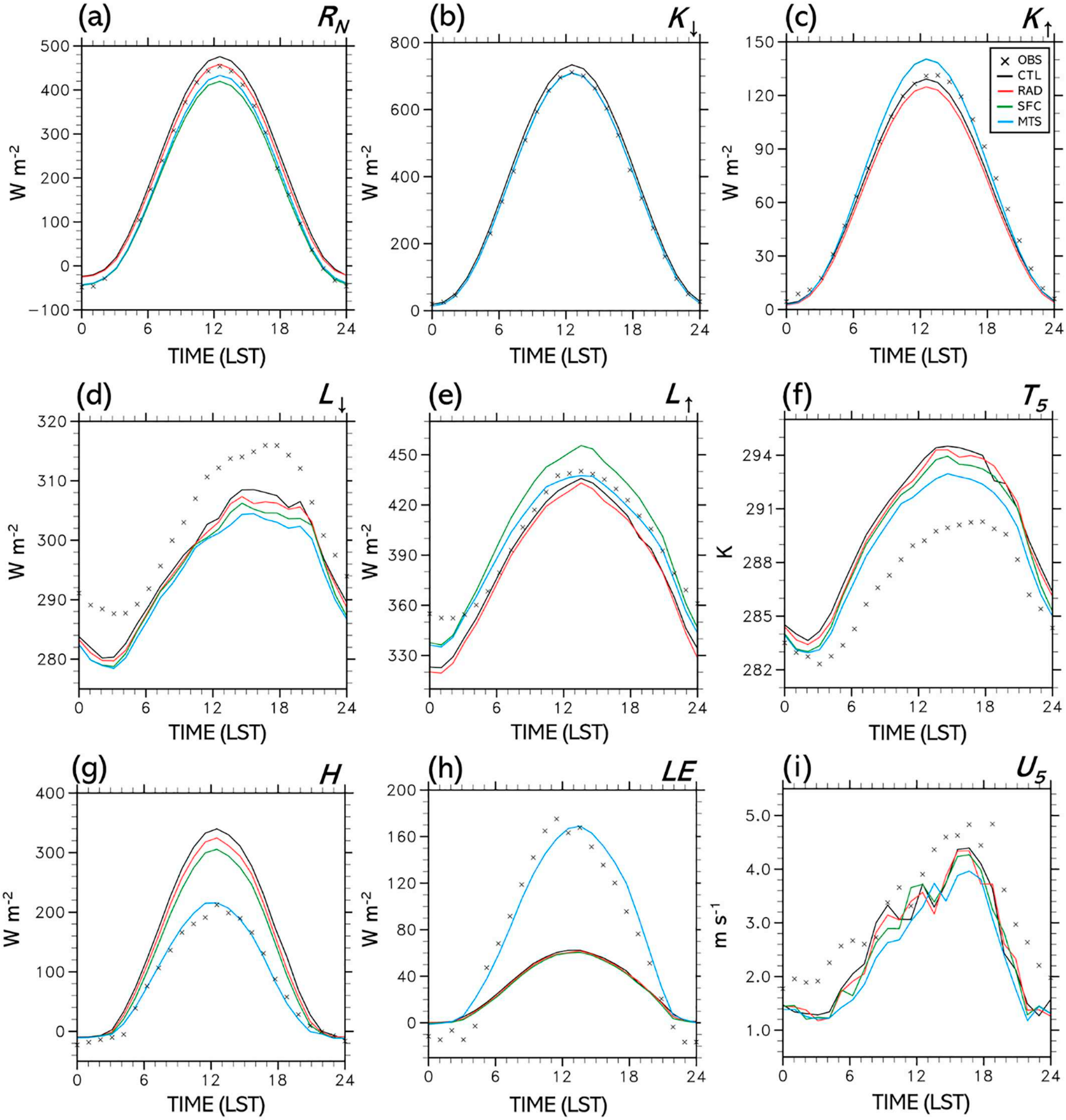

Fig. 2. Mean diurnal patterns of the surface variables simulated from CTL (black line), RAD (red line), SFC (green line), and MTS (blue line) experiments with observed data (x-dotted). Each graph shows (a) net radiation (R_N), (b) downward shortwave radiation ($K_\downarrow$), (c) upward shortwave radiation ($K_\uparrow$), (d) downward longwave radiation ($L_\downarrow$), (e) upward longwave radiation ($L_\uparrow$), (f) 5-m air temperature (T_5), (g) sensible heat flux (H), (h) latent heat flux (LE), and (i) 5-m wind speed (U_5). (For interpretation of the references to colour in this figure legend, the reader is referred to the web version of this article.)

period. In the CTL experiment (black line in Fig. 2), the PWRF reproduced the observed diurnal variability of surface radiative and energy fluxes ($R^2 \geq 0.86$). However, the model biases were large, especially in net radiation (R_N) and turbulent energy fluxes (i.e., H and LE) (Table 3). The correlation of $L_\downarrow$ was smaller because the PWRF did not capture the rapidly increasing rate in the morning and the timing of the daily minima (Fig. 2d). Except for $L_\downarrow$, all radiative fluxes contributed to overestimate R_N, that is, $K_\downarrow$ had a positive bias and all other components of surface radiative fluxes (i.e. $K_\uparrow$, $L_\downarrow$, and $L_\uparrow$) had negative biases in the simulation period.

The overestimations of R_N occurred mainly around noon and midnight, with the daytime overestimation of $K_\downarrow$ and nighttime underestimation of $L_\uparrow$ in the CTL experiment (Fig. 2). Previous studies reported similar overestimations of $K_\downarrow$ in atmospheric mesoscale models

Table 3
The simulating performance statistics of PWRF in each experiment. Values include bias (boldface), RMSE (italics) and correlation coefficient (parentheses) of surface variables.

VAR.	CTL	CTL_M	CTL_S	CTL_MS	RAD	RAD_M	RAD_S	RAD_MS	SFC	MTS
[a]$K_{\downarrow}$ (W m^{-2})	**17.5***20.2* (0.99)	**15.6***18.3* (0.99)	**14.9***17.4* (0.99)	**13.0***15.5* (0.99)	**0.5***6.3* (0.99)	**1.2***6.4* (0.99)	**−2.0***6.8* (0.99)	**−1.2***6.5* (0.99)	**0.8***6.4* (0.99)	**0.6***6.5* (0.99)
[b]$K_{\uparrow}$ (W m^{-2})	**−3.9***6.3* (0.99)	**−4.2***6.6* (0.99)	**−4.3***6.6* (0.99)	**−4.7***6.9* (0.99)	**−6.8***8.6* (0.99)	**−6.7***8.4* (0.99)	**−7.2***8.9* (0.99)	**−7.1***8.8* (0.99)	**1.1***6.0* (0.99)	**1.1***6.0* (0.99)
[c]$L_{\downarrow}$ (W m^{-2})	**−7.7***10.2* (0.86)	**−7.9***10.4* (0.86)	**−7.8***10.4* (0.86)	**−8.0***10.4* (0.85)	**−8.4***10.4* (0.87)	**−8.4***10.4* (0.86)	**−8.5***10.4* (0.86)	**−8.5***10.4* (0.86)	**−9.0***10.4* (0.87)	**−9.5***10.4* (0.86)
[d]$L_{\uparrow}$ (W m^{-2})	**−12.4***16.2* (0.97)	**−12.6***16.4* (0.97)	**−12.8***16.6* (0.97)	**−13.0***16.7* (0.97)	**−15.3***18.5* (0.97)	**−15.1***18.3* (0.97)	**−15.9***18.9* (0.97)	**−15.4***18.6* (0.97)	**6.2***14.0* (0.97)	**−2.3***10.0* (0.97)
[e]R_N (W m^{-2})	**26.5***27.7* (0.99)	**24.8***26.0* (0.99)	**24.6***25.9* (0.99)	**23.0***24.3* (0.99)	**14.6***17.3* (0.99)	**15.0***17.5* (0.99)	**13.0***16.4* (0.99)	**13.1***16.3* (0.99)	**−15.7***21.6* (0.99)	**−7.5***14.0* (0.99)
[f]H (W m^{-2})	**66.9***83.9* (0.99)	**65.3***82.3* (0.99)	**65.2***81.8* (0.99)	**63.8***80.3* (0.99)	**56.6***72.1* (0.99)	**57.0***72.8* (0.99)	**55.2***70.3* (0.99)	**55.2***70.7* (0.99)	**45.7***59.0* (0.99)	**3.3***15.2* (0.98)
[g]LE (W m^{-2})	**−43.3***64.9* (0.94)	**−43.4***65.0* (0.94)	**−43.4***65.0* (0.94)	**−43.6***65.1* (0.94)	**−44.3***65.7* (0.94)	**−44.3***65.7* (0.94)	**−44.4***65.7* (0.95)	**−44.4***65.8* (0.94)	**−45.1***66.1* (0.95)	**6.0***19.4* (0.97)
[h]T_5 (K)	**3.0***3.4* (0.93)	**2.9***3.4* (0.92)	**2.9***3.3* (0.92)	**2.9***3.3* (0.93)	**2.7***3.1* (0.94)	**2.7***3.2* (0.93)	**2.7***3.1* (0.93)	**2.7***3.1* (0.93)	**2.4***2.9* (0.93)	**1.9***2.4* (0.93)
[i]U_5 (m s^{-1})	**−0.5***1.1* (0.79)	**−0.6***1.1* (0.80)	**−0.5***1.1* (0.80)	**−0.6***1.1* (0.82)	**−0.6***1.1* (0.81)	**−0.6***1.1* (0.80)	**−0.6***1.1* (0.82)	**−0.6***1.1* (0.79)	**−0.7***1.2* (0.79)	**−0.8***1.3* (0.80)

[a] Downward shortwave radiation.
[b] Upward shortwave radiation.
[c] Downward longwave radiation.
[d] Upward longwave radiation.
[e] Net radiation.
[f] Sensible heat flux.
[g] Latent heat flux.
[h] 5-m air temperature.
[i] 5-m wind speed.

and attributed such overestimation to the lack of aerosol and ozone in the radiation schemes (e.g., Betts et al., 1997; Chen and Dudhia, 2001; Hong and Kim, 2008; Methymaki et al., 2018). In a PWRF study, Hines et al. (2011) also reported on the overestimation of $K_{\downarrow}$ during summer and concluded that the bias is related to a deficit of the simulated cloud fraction, which is not applicable in the present study because our analysis focused on clear-sky conditions. Our further sensitivity experiments indicated that the bias in $K_{\downarrow}$ can be reduced significantly with proper selection of radiation parameterization, model top, and the solar constant (see Subsection 3.2.1 for more discussion). Despite the overestimation $K_{\downarrow}$ in the model, $K_{\uparrow}$ was still underestimated and this indicates that the prescribed surface albedo in the model was smaller than the observed values and, accordingly, the surface albedo in the PWRF needs to be revised (Fig. 2c).

The underestimation of clear-sky $L_{\downarrow}$ is typically related to the cold bias of air temperature or the lack of water vapor in the model (e.g., Betts, 2009; Pinto et al., 1997). In particular, $L_{\downarrow}$ and thus net longwave radiation (LW_{net}) decrease if relative humidity (*RH*) is underestimated becase of the smaller clear-sky longwave greenhouse effect (Betts, 2009). In our study, the PWRF produced smaller *RH* and larger air temperature with the larger diurnal ranges of *RH* near the surface (Figs. 3 and 4). The warm bias partially contributed to the RH bias in the model but the model gave smaller mixing ratio in the PBL (Fig. S1). Indeed, the PWRF did not reproduce the observed relationship of the clear-sky LW_{net} with *RH*. Our findings suggest that humidity bias made substantial impact on clear-sky $L_{\downarrow}$ simulation where the solar zenith angle is large such as at arctic region similarly to Betts (2009).

It is also notable that the simulated atmospheric heating rate (i.e., increasing rate of T_5) was also greater than the observation in the morning under the influence of water vapor amount (Fig. 2f). We speculate that this is related to a smaller heat capacity near the earth surface in the model because the model underestimated water vapor having a larger heat capacity than the dry air. Our findings suggest that more accurate simulation of humidity is important in the Arctic region for longwave radiation and surface radiation balances.

For outgoing longwave radiation, the PWRF simulated less $L_{\uparrow}$ throughout the day and this negative bias became worse at night (Fig. 2e). Bias in $L_{\uparrow}$ was related to both the surface radiative and surface energy balances through surface temperature. Negative nocturnal bias in $L_{\uparrow}$ indicated excessive nighttime cooling on the surface in the model, which can be reduced by incorporating the organic layer into the model (Hines et al., 2011). Notably, our additional simulation gave a smaller bias in $L_{\uparrow}$ with changes in surface radiative properties and soil moisture (see Subsections 3.2.2 and 3.2.3 for more discussion).

The PWRF reproduced synoptic conditions near the surface in general. The simulated surface pressure showed a good performance with a bias of < 2 hPa and a correlation coefficient of 0.99 (not shown), which are within uncertainties in the terrain height between the model and observation. The simulated U_5 had a small negative bias of -0.5 m s^{-1} and a RMSE of 1.1 m s^{-1} with a correlation coefficient of 0.79 (Table 3). The performance of these variables are comparable with the PWRF performance reported by Hines et al. (2011). However, as the PWRF overestimated R_N, the model allocated more available energy to *H* than *LE* and these turbulent fluxes showed substantial biases against the observation; *H* showed a positive bias of 66.9 W m^{-2} whereas *LE* showed a negative bias of -43.3 W m^{-2}, leading to a larger Bowen ratio (i.e., $\beta > 5$) and higher air temperature in the PBL compared to the observation. With this bias in the SEB, the PWRF reproduced equivalent potential temperatures similar to the observation by a warmer (but drier) atmosphere with smaller saturation pressure height in the CTL experiment (Fig. 5a). Accordingly, it is probable that the cloud base was higher in the model compared to the observation. Our further analysis investigated potential sources of error of the PWRF in terms of uncertainties in input parameters and physical parameterizations.

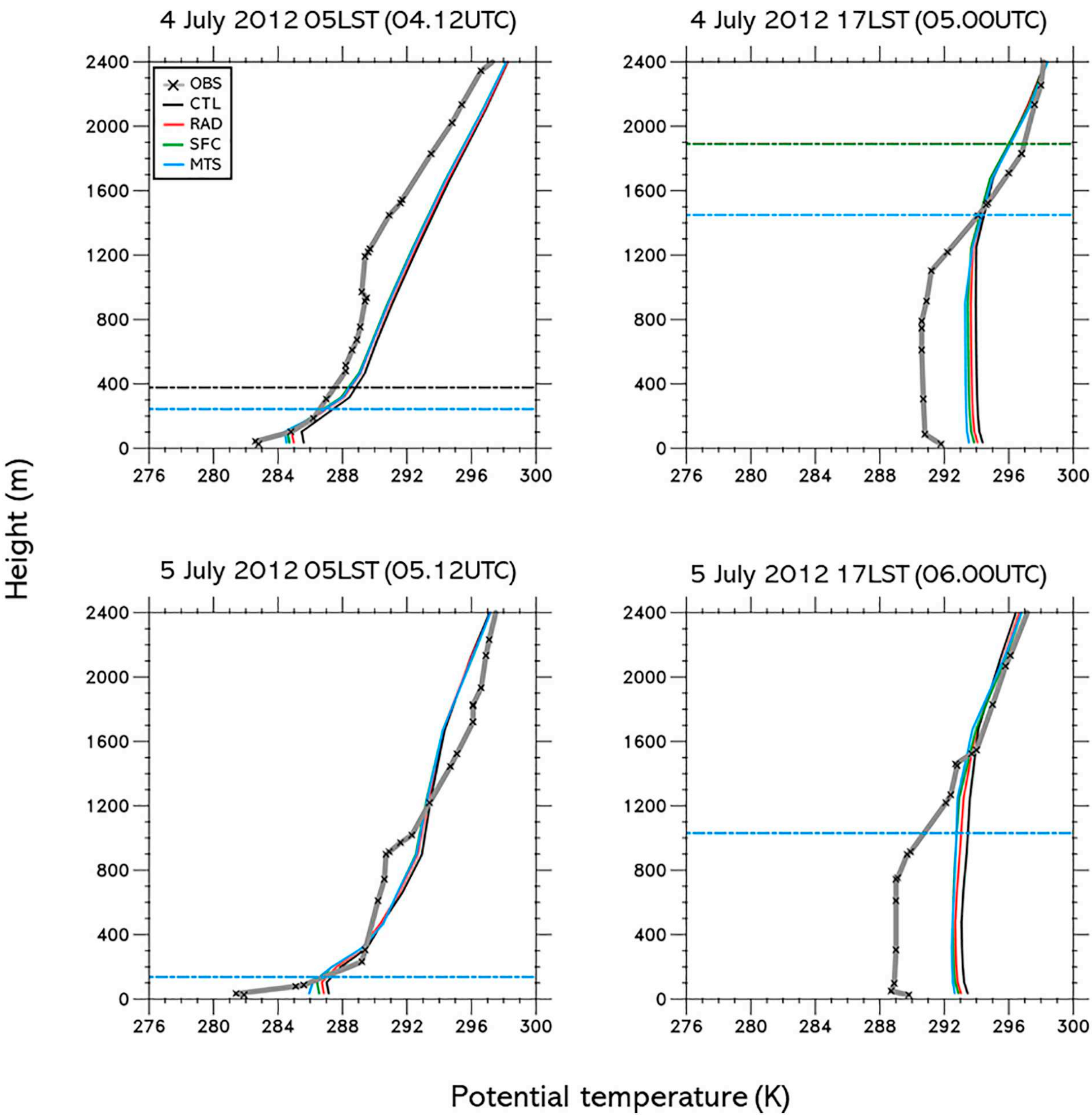

Fig. 3. Vertical potential temperature (θ) profile of CTL (black line), RAD (red line), SFC (green line), and MTS (blue line) experiments with radiosonde data (x-dotted gray line) for 4–6 July 2012 (12-hourly). The simulated PBL heights are plotted as horizontal dotted lines. (For interpretation of the references to colour in this figure legend, the reader is referred to the web version of this article.)

3.2. Sensitivity analysis

3.2.1. Downward shortwave radiation

The overestimation of $K_{\downarrow}$ in the CTL experiment was the main error source of overestimation of R_N during the daytime, which influences all surface energy fluxes eventually. Further sensitivity experiments were investigated to quantify the uncertainties of simulated $K_{\downarrow}$ with changes in the model top height, the solar constant, and radiative transfer schemes. It is clear that the simulated $K_{\downarrow}$ improved the model bias by from 1.9 to 4.5 W m^{-2} with the changes of model top height and the solar constant respectively compared to the CTL experiment, and its sensitivities were larger in the Goddard scheme (i.e. CTL) than in the RRTMG scheme (i.e. RAD) (Table 3).

Two radiation parameterizations overestimated $K_{\downarrow}$, however, the relative error was smaller in the RRTMG than in the Goddard parameterization. Bias and RMSE became 0.5 and 6.3 W m^{-2} in the RRTMG from 17.5 and 20.2 W m^{-2} in the Goddard scheme, respectively. Our results indicate that there was more radiative absorption in the RRTMG because of its broader and more spectral bands and more extinction sources (e.g., methane) than the Goddard (Ruiz-Arias et al., 2013). Notably, the RRTMG scheme produced increases in $K_{\downarrow}$ when the model top height increased, despite increases in the optical path, that was unlikely in the Goddard scheme. This suggests that multiple scattering is more active in the RRTMG. With the Goddard scheme (CTL), the positive bias of $K_{\downarrow}$ decreased to approximately 25% when a longer atmospheric depth (i.e., the model top set to 1 hPa: CTL_M) and the smaller solar constant (i.e., 1361 W m^{-2}: CTL_S) were used together (Table 3). Particularly, $K_{\downarrow}$ decreased mostly at noon when the RRTMG scheme is used (i.e., the RAD, SFC, and MTS experiments) (Fig. 2b).

The smaller solar constant (by 9 W m^{-2}, from 1370 to 1361 W m^{-2}) induced a decrease of approximately 2.5 W m^{-2} in surface $K_{\downarrow}$, regardless of the shortwave radiation parameterizations and the model top heights (Table 3). This finding indicates that a relatively shallow optical depth around the station results in substantial changes of

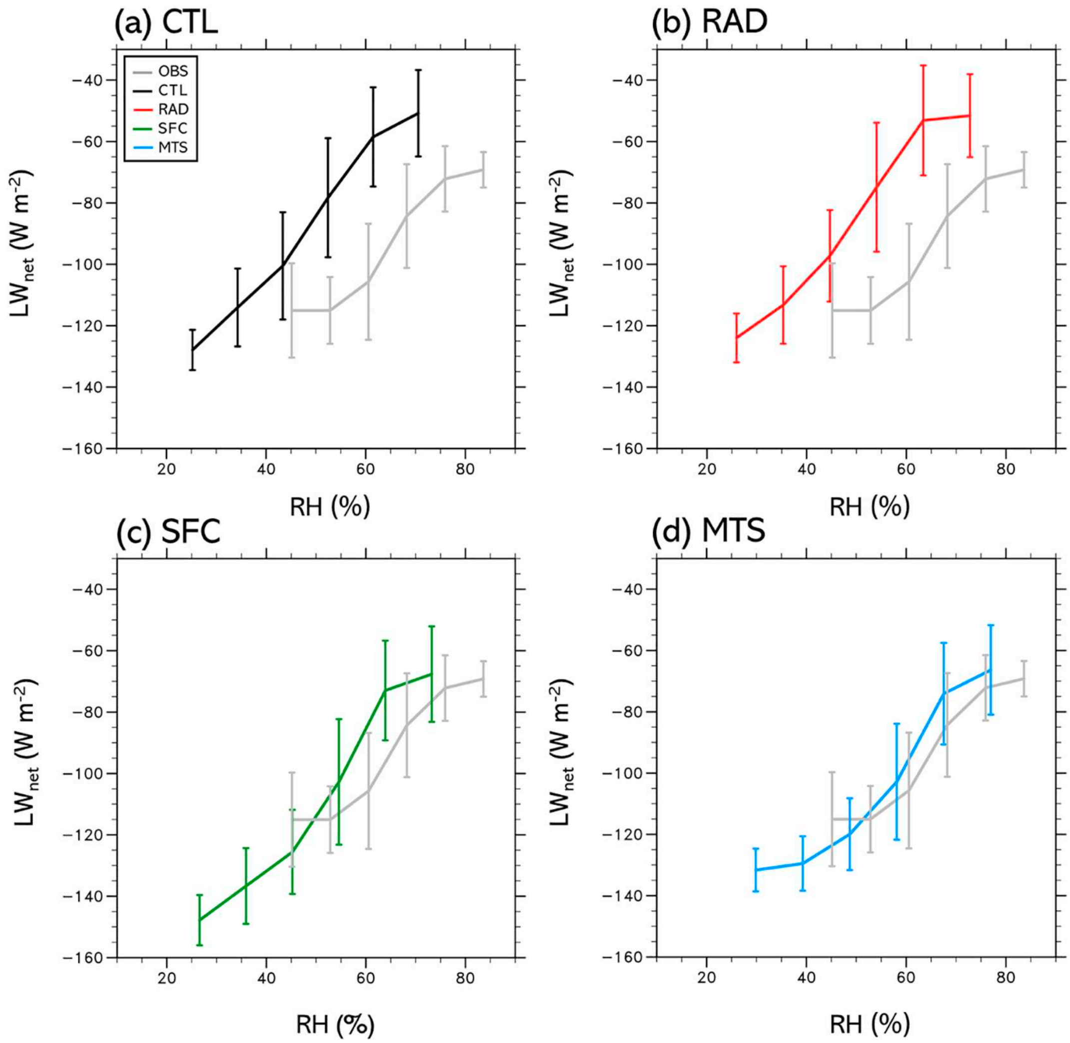

Fig. 4. Net longwave radiation (LW_{net}) with standard deviations binned by 5-m relative humidity (RH) for results of (a) CTL (black line), (b) RAD (red line), (c) SFC (green line), and (d) MTS (blue line) experiments with observation data (gray line). (For interpretation of the references to colour in this figure legend, the reader is referred to the web version of this article.)

surface incoming shortwave radiation with changes of the solar constant, and that uncertainty in the solar constant cannot be negligible over the Arctic area (Hong and Kim, 2008; Tosca et al., 2013).

Our results are consistent with previous WRF studies that reported improvement of surface shortwave radiative fluxes in the RRTMG parameterization (e.g., Ruiz-Arias et al., 2013; Wałaszek et al., 2014). Nevertheless, negative bias in $K_\uparrow$ and $L_\uparrow$ is exacerbated in the RAD experiment with the decreases of $K_\downarrow$, indicating that there are errors in surface albedo and emissivity of PWRF (red line in Fig. 2). Eventually, positive bias in R_N became smaller, by approximately 3.5 and 1.5 W m^{-2} in the CTL_MS and RAD_MS experiments, respectively, with the reduction of $K_\downarrow$ by the changes of the model top height and solar constant. Most of this R_N change is allocated to decreases in H with negligible changes in LE, leading to cooler air temperature in the PBL (red line in Fig. 3). Our findings indicate that careful selection of the radiation-related parameters and radiation schemes is necessary for the summer Arctic region.

3.2.2. Surface radiative parameters

Despite the improvement of $K_\downarrow$ in the RAD experiment, there were still large underestimations of $K_\uparrow$ and $L_\uparrow$ (red lines in Fig. 2c and e). Background surface albedo was prescribed with a daily variation in PWRF. The land cover corresponding to the footprint of the flux measurements was classified as a mixed tundra and the maximum and minimum values of surface albedo were set to 0.15 and 0.20 in the model, respectively, with surface emissivity of 0.92 in the PWRF. The daily surface albedo varied from 0.18 to 0.17 during the study period in the CTL experiment. An additional sensitivity simulation was performed by increasing the surface albedo to 0.20, based on the observation and surface emissivity of 0.98 reported at tundra sites (Langer et al., 2010, 2011; Wilber et al., 1999).

When surface albedo increased to 0.20 in the SFC experiment, bias of $K_\uparrow$ was reduced to 1.1 W m^{-2} (from −6.8 W m^{-2} in the RAD experiment), of which the magnitude corresponded to the positive bias of $K_\downarrow$ (Table 3). The increase of surface emissivity resulted in the parallel shift of $L_\uparrow$, leading to better performance, especially because of an improvement in the nighttime $L_\uparrow$ (green line in Fig. 2e). The bias of $L_\uparrow$ varied from −15.3 to 6.2 W m^{-2}, and the RMSE decreased from 18.5 to 14.0 W m^{-2}. In addition, LW_{net} and its relationship with RH provided a better agreement with the observation (Fig. 4c). Despite this improvement of $K_\uparrow$ and $L_\uparrow$ in the SFC experiment, there was no substantial improvement in the R_N simulation. The RMSE in R_N increased to 21.6 W m^{-2} in the SFC experiment from 17.3 W m^{-2} in the RAD experiment, and the bias in R_N changed from 14.6 to −15.7 W m^{-2} because of increases in $K_\uparrow$ and $L_\uparrow$ (Table 3). Consequently, the overestimation of H was reduced again by approximately 10 W m^{-2} without

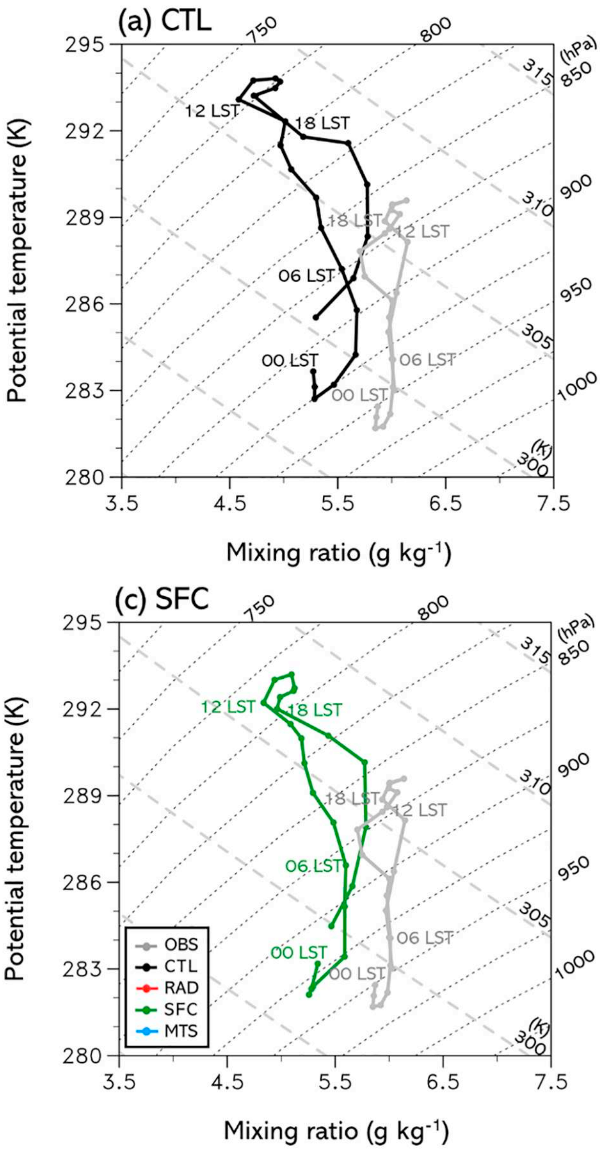

Fig. 5. Averaged diurnal cycle of potential temperature (***θ***) and mixing ratio (*q*) at the 5-m height of evaluation grid. The results of CTL (black line), RAD (red line), SFC (green line), and MTS (blue line) experiments are plotted with observed data (gray line). Gray dashed and thick gray dashed diagonal lines indicate the saturation pressure (short-dashed) and equivalent potential temperature (long-dashed), respectively. (For interpretation of the references to colour in this figure legend, the reader is referred to the web version of this article.)

changes in *LE*, compared to the RAD experiment. Furthermore, the SFC experiment also reduced the bias of air temperature in the convective mixed layer by approximately 1 °C (green line in Fig. 3).

3.2.3. Soil water content

The observed monthly mean of soil water content in July 2012 was approximately 0.28 $m^3\ m^{-3}$ in CBB. Initial soil moisture content from the ERA-Interim and thus the PWRF simulated a lower soil water content than the observed value in the top soil layer (0.15–0.20 $m^3\ m^{-3}$) from the beginning of the simulation (Fig. 6a). An additional 10-year recursive spin-up run was carried out for initial soil moisture content with the offline Noah LSM based on Koster et al. (2009) and Lim et al. (2012). Notably, soil moisture quickly converged to the equilibrium state in one year the spin-up time and the equibrium soil moisture content was similar with the observed value (Fig. S2). Accordingly, we speculate that such smaller initial condition of soil moisture is related to the spin-up of a land surface model rather than physical processes such as the thawing and drainage processes in summer Arctic tundra. In this perspective, the additional sensitivity experiment (MTS; Moist Top Soil) was designed with the observed monthly mean soil water content to quantify error of the SEB due to soil moisture. Hines et al. (2011) reported a minor influence of soil water content over the Arctic region based on increases of the initial soil moisture content. If we only increased initial soil moisture value, the soil moisture content rapidly decreased to approximately 0.20 $m^3\ m^{-3}$ within a few days resulting in lower soil moisture in the model and did not produced substantial changes of SEB (not shown). Accordingly, in the MTS experiment, our study designed that soil water content in the top soil layer is fixed to the monthly mean value of soil water content in the innermost domain (68.9–69.3°N, 104.4–105.5°W) (i.e., 0.28 $m^3\ m^{-3}$).

The Taylor diagram showed that the overall performances of all variables improved in the MTS experiment particularly in *H* and *LE* (Fig. 7). With the increased soil water content, the *LE* increased whereas *H* decreased substantially, thus leading to a good agreement of β with the observation. The bias of *H* and *LE* decreased substantially from 45.7 and −45.1 W m^{-2} in SFC experiment to 3.3 and 6.0 W m^{-2} respectively (Table 3). The increase in *LE* produced a lower surface temperature and $L_{\uparrow}$ accordingly (Table 3 and Fig. 2e). With the

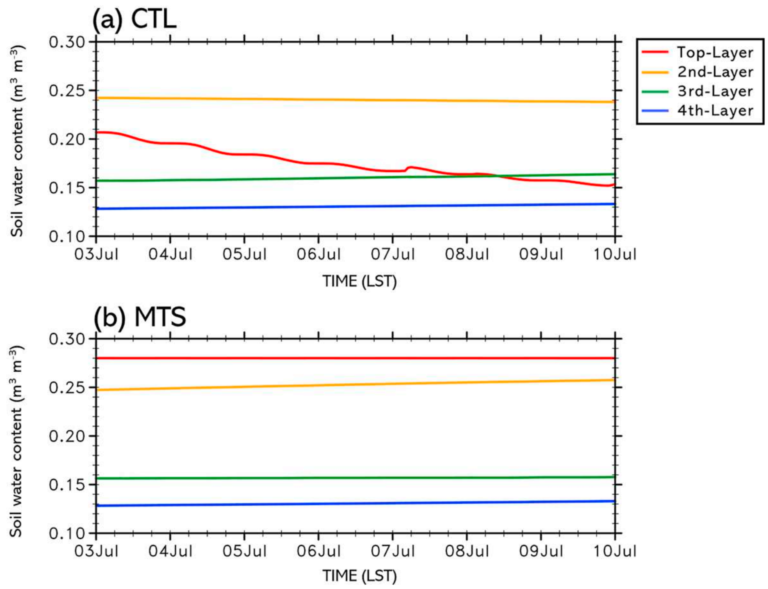

Fig. 6. Soil water content in soil layers from (a) the CTL and (b) MTS experiments.

improvement of SEB in the MTS experiment, the T_5 simulation also improved because of its decreases (Fig. 2f), and the relationship of RH and LW_{net} was well reproduced (Fig. 4d). Vertical profiles of θ in the PBL still indicated a warm bias in the MTS, however it became smaller in the MTS experiment (blue line in Figs. 3–5). The U_5 was not influenced by soil moisture with the similar bias and correlation coefficient. The steeper decreasing rate of soil water content, which can be attributable to error in soil heat capacity and soil hydraulic conductivity, was also mitigated in the MTS experiement (Fig. 6). This is because soil heat capacity is proportional to soil water content and increased with increased soil moisture in the MTS experiment. Eventually, this also mitigated the steeper changing rate of $L_{\uparrow}$ during the daytime, which is also related to the surface temperature with the decrease in its daily maxima (Fig. 2e).

Betts (1992, 2009) showed that the vector change in the mixing diagram is decided by the SEB and entrainment fluxes at the PBL top. If we consider that the MTS reproduced the observed β and the magnitudes of H and LE, the bias of diurnal change in the mixing diagram in the MTS experiment indicated potential error in the entrainment fluxes (Fig. 5d). Our results indicate that the spin-up of soil water content and soil hydraulic properties have critical roles in the Arctic SEB and temperature and humidity in the PBL, in addition to the improved initial condition of soil moisture content.

4. Summary and conclusions

Arctic tundra is likely to be exposed to warmer conditions with a warming global climate. This study evaluated the simulation performance of PWRF over the Arctic tundra region on clear summer days based on in-situ observations of the SEB and PBL structure. Our analysis placed emphasis on the model performance on non-cloudy days over the summer Arctic tundra to investigate the performance of PWRF without the bias of cloud in the model. Overall, PWRF simulated a good diurnal pattern of surface variables on non-cloudy days. Despite these

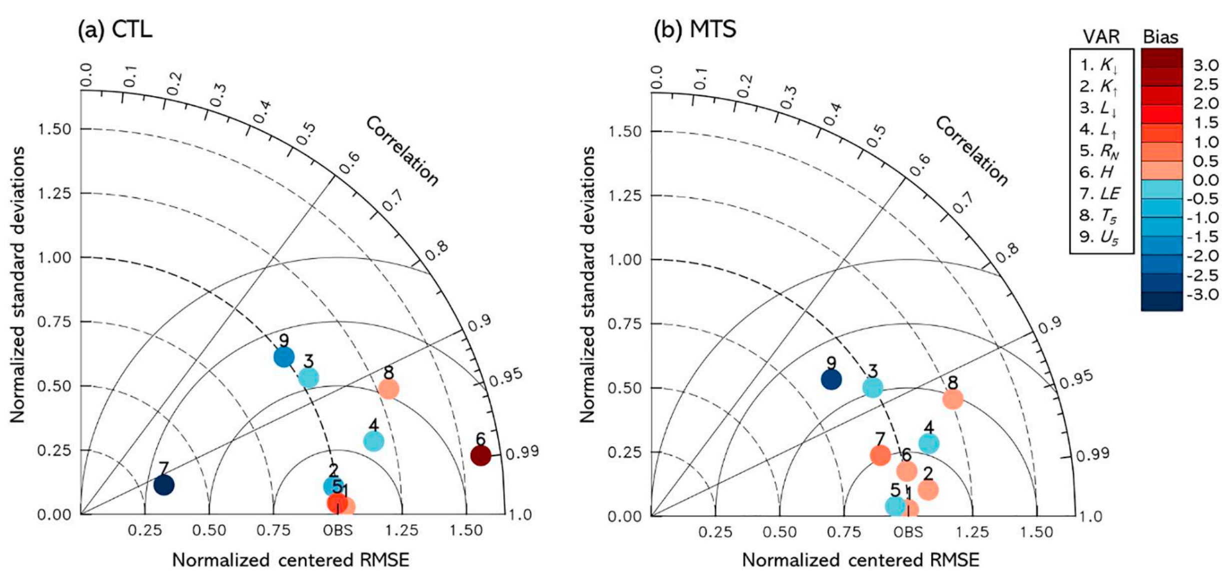

Fig. 7. Taylor diagram of surface variables from CTL (black) and MTS (blue) experiments comparing with observed data. The normalized bias, standard deviations and centered-RMSE, and correlation coefficient are plotted. (For interpretation of the references to colour in this figure legend, the reader is referred to the web version of this article.)

large correlations with observations, PWRF simulated a different SEB from the observation on the clear summer days, leading to a warmer PBL environment. The $K_{\downarrow}$ was overestimated at midday and the other $K_{\uparrow}$, $L_{\downarrow}$, and $L_{\uparrow}$ were underestimated in the model, leading to the overestimation of R_N by 27 W m^{-2}. With this overestimation of R_N in the model in drier conditions, the more available energy is partitioned to H than LE. Indeed, H had a positive bias of 66.9 W m^{-2} whereas LE was underestimated with a negative bias of -43.3 W m^{-2}.

Sensitivity analysis was conducted to quantify the model bias induced by uncertainties in surface parameters and model design. Our sensitivity analysis clearly shows that the surface radiation balance depends on the atmospheric radiation scheme with the solar constant and model top height, surface albedo, and surface emissivity. Despite improvements of surface radiation with their proper assignment, they did not improve the surface energy partitioning of R_N into H and LE. Further analysis showed that bias in the soil moisture content plays a critical role in regulating the surface energy partitioning by reducing warm and dry bias in the model. With the increases in soil moisture during the whole simulation period, the RMSE of H and LE were decreased by approximately 80% and 70%, respectively, each from the CTL experiment. Our findings propose that the PWRF can capture temporal evolution of the SEB and PBL structure in non-cloudy conditions if the radiation physics and surface parameters are properly selected with reliable simulation of soil moisture. Notably, our results corroborated that the model captured the SEB not only with realistic initial conditions of soil moisture contents, but also that proper soil hydraulic and thermal properties are necessary. It is also notable that despite this substantial improvement, $L_{\downarrow}$ showed a negative bias in all the simulations, possibly due to water vapor in the atmosphere, and air temperature and humidity in the PBL had bias possibly due to improper simulation of the entrainment fluxes in the PBL top based on the mixing chart analysis. Our study suggests that we should carefully decide on the numerical experimental design in the Arctic region and emphasize field measurement of vegetation and cover in this sentive area to climate changes. Furthermore, additional evaluation studies should be conducted to focus on interactions between the PBL and its overlying free atmosphere and longwave radiation processes over the Arctic area to improve modeling.

Declaration of Competing Interest

The authors declare that they have no known competing financial interests or personal relationships that could have appeared to influence the work reported in this paper.

Acknowledgements

This research was supported by a National Research Foundation of Korea Grant from the Korean Government (MSIT) (NRF-2017M1A5A1013567) (NRF-2016M1A5A1901769, KOPRI-PN20081) and (NRF-2018R1A5A1024958), and the Korea Meteorological Administration Research and Development Program under Grant KMI2018-03512. The first author was supported by Hyundai Motor Chung Mong-Koo Foundation. Our thanks go to the Byrd Polar Research Center at the Ohio State University for making the PWRF available.

Appendix A. Supplementary data

Supplementary data to this article can be found online at https://doi.org/10.1016/j.atmosres.2020.104946.

References

Anisimov, O., 2007. Potential feedback of thawing permafrost to the global climate system through methane emission. Environ. Res. Lett. 2 (4), 45016.

Beitler, J., 2012. Arctic sea ice extent settles at record seasonal minimum. In: Arctic Sea Ice News and Analysis. National Snow and Ice Data Center. *http://nsidc.org/arcticseaicenews/2012/09/arctic-sea-ice-extent-settles-at-record-seasonal-minimum*.

Betts, A., 1992. FIFE atmospheric boundary layer budget methods. J. Geophys. Res.-Atmos. 97, 18523–18532.

Betts, A., 2009. Land-surface-atmosphere coupling in observations and models. J. Adv. Model. Earth Syst. 1, 4. https://doi.org/10.3894/JAMES.2009.1.4.

Betts, A., Chen, F., Mitchell, K., Janjić, Z., 1997. Assessment of land surface and boundary layer models in two operational versions of the Eta model using FIFE data. Mon. Weather Rev. 125, 2896–2915.

Bromwich, D.H., Hines, K.M., Bai, L.S., 2009. Development and testing of polar weather research and forecasting model: 2. Arctic Ocean. J. Geophys. Res.-Atmos. 114 (D8).

Bromwich, D., Wilson, A., Bai, L., Liu, Z., Barlage, M., Shih, C.-F., et al., 2018. The arctic system reanalysis, version 2. Bull. Am. Meteorol. Soc. 99 (4), 805–828.

Calihoo, C., Romaine, T., 2010. Climate Change Adaptation Action Plan for Cambridge Bay. In: Cambridge Bay.

Cavalieri, D.J., Parkinson, C.L., 2012. Arctic sea ice variability and trends, 1979-2010. Cryosphere 6 (4), 881.

Chapin III, F.S., Eugster, W., McFadden, J.P., Lynch, A.H., Walker, D.A., 2000. Summer differences among arctic ecosystems in regional climate forcing. J. Clim. 13, 2002–2010.

Chen, F., Dudhia, J., 2001. Coupling an advanced land surfacehydrology model with the Penn State-NCAR MM5 modeling system, Part II: preliminary model validation. Mon. Weather Rev. 129, 587–604.

Christensen, T.R., Johansson, T., Åkerman, H.J., Mastepanov, M., Malmer, N., Friborg, T., et al., 2004. Thawing sub-arctic permafrost: Effects on vegetation and methane emissions. Geophys. Res. Lett. 31 (4).

Cohen, J., Screen, J.A., Furtado, J.C., Barlow, M., Whittleston, D., Coumou, D., et al., 2014. Recent Arctic amplification and extreme mid-latitude weather. Nat. Geosci. 7 (9), 627.

Comiso, J.C., Parkinson, C.L., Gersten, R., Stock, L., 2008. Accelerated decline in the Arctic Sea ice cover. Geophys. Res. Lett. 35 (1).

Elmendorf, S.C., Henry, G.H., Hollister, R.D., Björk, R.G., Bjorkman, A.D., Callaghan, T.V., et al., 2012. Global assessment of experimental climate warming on tundra vegetation: heterogeneity over space and time. Ecol. Lett. 15 (2), 164–175.

Elvidge, S., Angling, M., Nava, B., 2014. On the use of modified Taylor diagrams to compare ionospheric assimilation models. Radio Sci. 49 (9), 737–745.

Eugster, W., Rouse, W.R., Pielke Sr., R.A., McFadden, J.P., Baldocchi, D.D., Kittel, T.G.F., Chapin III, F.S., Liston, G.E., Vidale, P.L., Vaganov, E., Chambers, S., 2000. Land–atmosphere energy exchange in Arctic tundra and boreal forest: available data and feedbacks to climate. Glob. Chang. Biol. 6, 84–115.

Goetz, S.J., Epstein, H.E., Bhatt, U.S., Jia, G.J., Kaplan, J.O., Lischke, H., et al., 2010. Recent changes in arctic vegetation: satellite observations and simulation model predictions. In: Eurasian Arctic Land Cover and Land Use in a Changing Climate. Springer, pp. 9–36.

Henry, G., Molau, U., 1997. Tundra plants and climate change: the International Tundra Experiment (ITEX). Glob. Chang. Biol. 3 (S1), 1–9.

Hines, K.M., Bromwich, D.H., 2008. Development and testing of Polar Weather Research and forecasting (WRF) model. Part I: Greenland ice sheet meteorology. Mon. Weather Rev. 136 (6), 1971–1989.

Hines, K.M., Bromwich, D.H., Bai, L.-S., Barlage, M., Slater, A.G., 2011. Development and testing of Polar WRF. Part III: Arctic land. J. Clim. 24 (1), 26–48.

Hines, K.M., Bromwich, D.H., Bai, L., Bitz, C.M., Powers, J.G., Manning, K.W., 2015. Sea ice enhancements to Polar WRF. Mon. Weather Rev. 143 (6), 2363–2385.

Hinzman, L.D., Bettez, N.D., Bolton, W.R., Chapin, F.S., Dyurgerov, M.B., Fastie, C.L., Griffith, B., Hollister, R.D., Hope, A., Huntington, H.P., Jensen, A.M., 2005. Evidence and implications of recent climate change in northern Alaska and other arctic regions. Clim. Chang. 72 (3), 251–298.

Hong, J., Kim, J., 2008. Scale-dependency of surface fluxes in an atmospheric mesoscale model: effect of spatial heterogeneity in atmospheric conditions. Nonlinear Process. Geophys. 15, 965–975.

Koster, R.D., Guo, Z., Yang, R., Dirmeyer, P.A., Mitchell, K., Puma, M., 2009. On the nature of soil moisture in land surface models. J. Clim. 4322–4335.

Langer, M., Westermann, S., Boike, J., 2010. Spatial and temporal variations of summer surface temperatures of wet polygonal tundra in Siberia-implications for MODIS LST based permafrost monitoring. Remote Sens. Environ. 114 (9), 2059–2069.

Langer, M., Westermann, S., Muster, S., Piel, K., Boike, J., 2011. The surface energy balance of a polygonal tundra site in northern Siberia Part 1: Spring to fall. Cryosphere 5, 151–171.

Lee, B.Y., 2018. Circum Arctic Permafrost Environment Change Monitoring, Future Prediction and Development Techniques of Useful Biomaterials (CAPEC).

Lim, Y.J., Hong, J., Lee, T.Y., 2012. Spin-up behavior of soil moisture content over East Asia in a land surface model. Meteorog. Atmos. Phys. 118, 151–161.

Lynch, A.H., Chapman, W.L., Walsh, J.E., Weller, G., 1995. Development of a regional climate model of the western Arctic. J. Clim. 8 (6), 1555–1570.

Lynch, A.H., McGinnis, D.L., Bailey, D.A., 1998. Snow-albedo feedback and the spring transition in a regional climate system model: Influence of land surface model. J. Geophys. Res.-Atmos. 103 (D22), 29037–29049.

Methymaki, G., Bossioli, E., Dandou, A., Kalogiros, J., Biskos, G., Mihalopoulos, N., Nenes, A., Tombrou, M., 2018. Solar irradiance prediction over the Aegean Sea: shortwave parameterization schemes and aerosol radiation feedback. In: Mensink, C., Kallos, G. (Eds.), Air Pollution Modeling and its Application XXV. ITM 2016. Springer Proceedings in Complexity. Springer, Cham.

Overland, J., Francis, J.A., Hall, R., Hanna, E., Kim, S.-J., Vihma, T., 2015. The melting Arctic and midlatitude weather patterns: are they connected? J. Clim. 28 (20), 7917–7932.

Parkinson, C.L., Comiso, J.C., 2013. On the 2012 record low Arctic Sea ice cover:

combined impact of preconditioning and an August storm. Geophys. Res. Lett. 40 (7), 1356–1361.
Pinto, J.O., Curry, J.A., Fairall, C.W., 1997. Radiative characteristics of the Arctic atmosphere during spring as inferred from ground-based measurements. J. Geophys. Res.-Atmos. 102 (D6), 6941–6952.
Roberts, A., Cassano, J., Döscher, R., Hinzman, L., Holland, M., Mitsudera, H., et al., 2010. A Science Plan for Regional Arctic System Modeling. A report to the National Science Foundation from the International Arctic Science Community, In.
Ruiz-Arias, J.A., Dudhia, J., Santos-Alamillos, F.J., Pozo-Vázquez, D., 2013. Surface clear-sky shortwave radiative closure intercomparisons in the Weather Research and Forecasting model. J. Geophys. Res.-Atmos. 118 (17), 9901–9913.
Serreze, M.C., Barry, R.G., 2014. The Arctic Climate System. Cambridge University Press.
Taylor, K.E., 2001. Summarizing multiple aspects of model performance in a single diagram. J. Geophys. Res.-Atmos. 106 (D7), 7183–7192.
Tosca, M.G., Randerson, J.T., Zender, C.S., 2013. Global impact of smoke aerosols from landscape fires on climate and the Hadley circulation. Atmos. Chem. Phys. 13, 5227–5241.
Twine, T.E., Kustas, W., Norman, J., Cook, D., Houser, P., Meyers, T., et al., 2000. Correcting eddy-covariance flux underestimates over a grassland. Agric. For. Meteorol. 103 (3), 279–300.
Wałaszek, K., Kryza, M., Werner, M., 2014. A sensitivity analysis of the WRF model to shortwave radiation schemes for air quality purposes and evaluation with observational data. In: Air Pollution Modeling and its Application XXIII. Springer, pp. 539–543.
Weisman, M.L., Skamarock, W.C., Klemp, J.B., 1997. The resolution dependence of explicitly modeled convective systems. Mon. Weather Rev. 125 (4), 527–548.
Wilber, A.C., Kratz, D.P., Gupta, S.K., 1999. Surface Emissivity Maps for Use in Satellite Retrievals of Longwave Radiation.
Wilson, A.B., Bromwich, D.H., Hines, K.M., 2011. Evaluation of Polar WRF forecasts on the Arctic System Reanalysis domain: Surface and upper air analysis. J. Geophys. Res.-Atmos. 116 (D11).
Wilson, A.B., Bromwich, D.H., Hines, K.M., 2012. Evaluation of Polar WRF forecasts on the Arctic System Reanalysis domain: 2. Atmospheric hydrologic cycle. J. Geophys. Res.-Atmos. 117 (D4).
Woods, T.N., Rottman, G.J., Harder, J.W., Lawrence, G.M., McClintock, W.E., Kopp, G.A., Pankratz, C., 2000. Overview of the EOS SORCE mission. In: Paper presented at the Earth Observing Systems V.